Tongue Image Alignment via Conformal Mapping for Disease Detection

JIAN WU[1], **BOB ZHANG**[2], **(Senior Member, IEEE), YONG XU**[1,4]**, (Senior Member, IEEE), AND DAVID ZHANG**[3,5]**, (Fellow, IEEE)**

[1]School of Computer Science and Technology, Harbin Institute of Technology at Shenzhen, Shenzhen 518055, China
[2]Department of Computer and Information Science, University of Macau, Macau, China
[3]School of Science and Engineering, The Chinese University of Hong Kong at Shenzhen, Shenzhen 518172, China
[4]Peng Cheng Laboratory, Shenzhen 518000, China
[5]Shenzhen Research Institute of Big Data, Shenzhen 518172, China

Corresponding author: Jian Wu (wujianhitsz@gmail.com)

ABSTRACT Tongue image analysis has been an active study in medical imaging. Existing tongue image processing approaches deal with the issue of image alignment in oversimplified ways. These approaches mainly extract patches or simple regions on pre-defined positions, which are severely sensitive to tongue deformations. In this paper, we present a conformal mapping method for tongue image alignment, the principle of which is to determine the interior mapping based on the boundary mapping so that it is robust to the deformations. The conformal alignment consists of two stages: the mapping on the boundary is firstly established via the Fourier descriptor before the mapping is extended onto the interior region via Cauchy's integral and finite-difference method. Average tongues and eigen-tongues are constructed based on the conformal alignment for feature extraction. Experiments show that the proposed alignment is robust against tongue deformations and can be employed to correct existing rigid partition methods. Numerical evaluations on time efficiency and accuracy also show that our method is considerably fast and very accurate, compared with several baseline methods in this field. For the task of disease detection, the features based on the aligned images outperform some state-of-the-art features. The results reveal that the proposed method provides an efficient and accurate tool for deformable medical image alignment and disease diagnosis. A MatLab script of the proposed algorithm is available on `https://codeocean.com/capsule/4382908/tree/v1`.

INDEX TERMS Image alignment, conformal mapping, disease detection.

I. INTRODUCTION

Tongue imaging has caused increasing research interests in the last two decades [1]–[14]. Compared with mainstream medical imaging approaches, tongue image analysis has the advantages of cheap and convenient imaging yet accurate diagnosis [3]–[5], [10].

Image registration/alignment is known as matching the points or features between two taken pictures [15], [16]. The alignment of tongue images[1] can also be defined as establishing mappings of the points or sub-regions among different tongue images. Tongue image alignment is a fundamental issue to tongue diagnosis. In fact, the tongue surface usually shows various appearances according to the spot locations [1], [9]. For instance, the tongue tip is relatively more reddish and smooth than the other parts [9], [11], while the area near the tongue root is usually covered by coatings of various colors [6], [8].

The aim of the tongue image alignment is to serve as a utility tool for many applications. Actually, many well-known image learning methods are based on the assumption that the underlying images are aligned, including sparse representation classification [17], eigenface [18], fisherface [19], and Laplacianface [20]. Hence, theoretically speaking, the aforementioned methods can be applied on the tongue images once they have been aligned. Actually, in this work we will discuss the application of tongue image alignment

---

The associate editor coordinating the review of this manuscript and approving it for publication was Kumaradevan Punithakumar.

[1]Throughout the paper, we mean the alignment of tongue body/region in the image when we speak of *tongue image alignment* or *alignment of tongue images*, where the tongue body/region has been segmented from the background before the alignment.
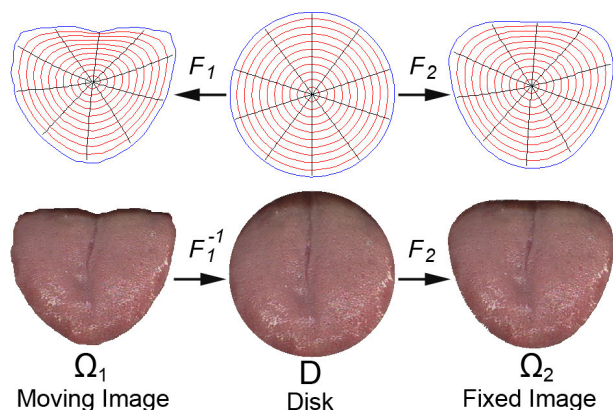
FIGURE 1. Gist of the proposed alignment method via conformal mappings: F_1 and F_2 are Riemann mappings from the unit disk onto moving and fixed images respectively and F_1^{-1} is the inverse mapping of F_1. The compound $F_2 \circ F_1^{-1}$ is the conformal mapping between the moving and the fixed images.

in feature extraction, region partition, and eigen-image construction.

The tongue image alignment faces significant challenges. One challenge is that the tongue shape is highly unpredictable [21], [22]. As a result, any predefined or fixed tongue location approach is vulnerable to the attack of tongue deformations. Another challenge lies in the alignment between the tongues of different individuals. In fact, there are few coherent subject matters on the tongue surfaces to guide the alignment. Although sometimes the cracks and papillae on the tongue surfaces can serve as the subject matters, however those features are not always available in all cases.

Most existing approaches on the issue of tongue alignment are oversimplified. Some approaches partition the tongue region into several simple pieces [1], [3], [6], while others crop some patches on a few specific locations [4], [10], [11]. These methods suffer from some disadvantages. Firstly, the mappings of these methods are discrete, processing only a few points or sub-regions in the tongue region. Secondly, these methods are based the assumption of vertical tongues, which is not always the case in the real-world practices. As a result, these methods are vulnerable to tongue deformation attacks.

The main goal of this work is to establish dense and flexible mappings between tongue images. Despite the fact that the aforementioned approaches deal with few isolated points/sub-regions on the tongue surface, the proposed mapping is a point-to-point surjection, which covers all the pixels in the tongue regions. Besides this, the proposed method can handle the dramatic deformation of the tongue shapes. The solution is motivated by the celebrated Cauchy's integral formula of conformal mappings, where the mapping of the interior points is determined by the mapping of the region shapes. In another words, the edge points are used as the alignment landmarks. The gist of our method is visualized in Fig. 1, where the moving and fixed images are firstly mapped onto a disk domain via the Riemann mappings and then the mapping between the tongues is the compound of the two Riemann mappings.

The proposed method is divided into two stages: boundary corresponding and analytic extension. In the boundary corresponding stage, an analytic mapping is constructed between the unit circle and the tongue boundary. This procedure is implemented by the Fourier descriptor. In the analytic extension stage, the mapping on the boundary is extended onto the interior region. The mapping on the interior is firstly calculated by Cauchy's integral formula, which is numerically instable and then the numerical instability is recursively improved by finite-difference methods. The main contributions of this work contains:

- We introduce conformal mappings as diffeomorphisms to tackle the issue of the alignment of deformable tongue images.
- The conformal mapping computation is accelerated via a two-stage strategy of boundary corresponding and analytic extension, which is more accurate than several classic and recent methods.
- Based on conformal alignment, we propose the concepts of average tongue and eigen-tongue, which provide helpful tools for functional sectorization analysis.

Throughout this paper, experiments are performed on a tongue image dataset with 3,980 images. However, our method can be broadly applied to other medical image alignments. Experimental results show that our method outperforms many state-of-the-art packages on accuracy. Moreover, the features based on eigen-tongues improve the performance of tongue diagnosis in disease detection.

II. RELATED WORKS
A. FUNCTIONAL SECTORIZATIONS OF TONGUE
Alignment studies on tongue image are less sophisticated. The principle of these works is to extract several predefined key points on the tongue region, or to partition the tongue region into several sub-regions. Some works [1], [3], [6] divide the tongue surface into several regions with straight boundaries. Other works [4], [10], [11] extract from the tongue surface several blocks. The gist of these methods is visualized in Fig. 2, where the figures are directly quoted from the involved articles. We argue that these approaches suffer from a severe difficulty. Actually they treat the tongue as a rigid body and implicitly demand that the tongue body must be vertically oriented, as is demonstrated in Fig. 2. The assumption is artificial and unnecessary to the deformability of a tongue in nature.

B. IMAGE ALIGNMENTS AND REGISTRATIONS
Image registration is an active topic in the field of scene images [23]–[26] and formable medical images [27]–[29]. These methods usually establish diffeomorphisms between images [26]- [28]. The principle of these methods is to solve the Euler-Lagrange equations of some object functionals [23], [26], thus images are successively deformed following some displacement flows. However this category of methods implicitly demands some supervised information
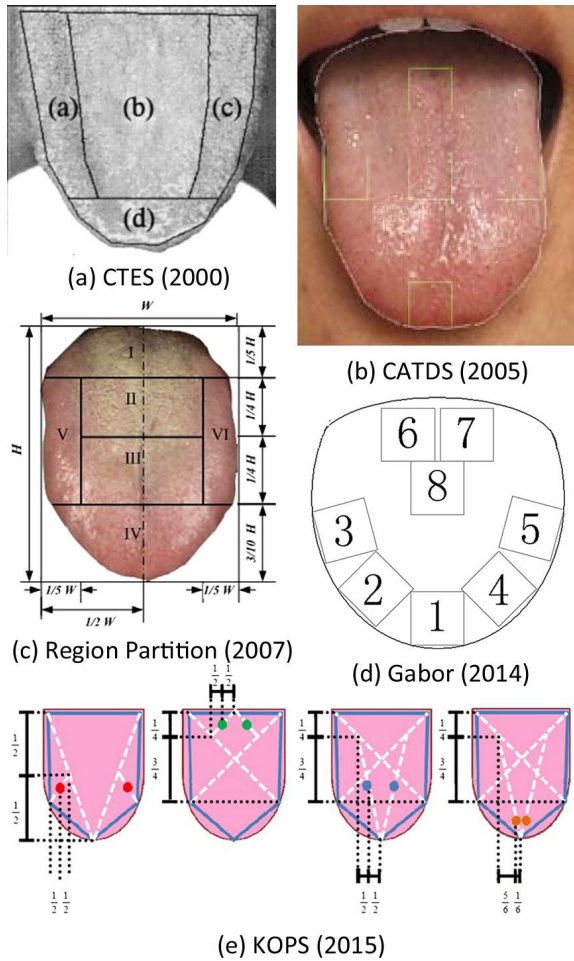
(a) CTES (2000)

(b) CATDS (2005)

(c) Region Partition (2007)

(d) Gabor (2014)

(e) KOPS (2015)

FIGURE 2. Some existing methods of tongue alignment. The images are respectively quoted from [1](CTES), [5](CATDS), [6](Region Partition), [10](Gabor), and [11](KOPS).

on the images to mark the displacement flow, which adds up extra work loads for the unsupervised tasks. For example, the optical flow approaches [23] use intensity as supervising information to track displacement flows. Another type of image registration/alignment methods belongs to the category of deep learning [29]–[32]. This group of schemes does not need the supervised information and usually performs very well on some large scaled tasks. However, the performance of these methods heavily relies on some preconditions as follows: advantageous hardware, huge training dataset, and an extensive training time.

C. CONFORMAL MAPPINGS
Conformal mappings are firstly known as transformations between regions in complex planes and then later developed into mappings between differential manifolds, especially 3d surfaces. This category of mappings has a nice property of preserving the orientation and angle locally. There have been extensive studies on the computation of conformal mappings [33]–[37] and in the applications of surface matching, registration, shape analysis, etc. [38]–[41], [43], [44]

III. PROPOSED METHOD
This section is devoted to present a conformal mapping approach for tongue image alignment. We firstly introduce the motivation and the algorithmic framework and then describe each procedure in the framework. The framework is comprised of three procedures, including boundary corresponding, analytic extension, and finite-difference method.

A. MOTIVATION
Diffeomorphisms are widely used as alignment mappings between images [26]–[28], since they preserve local structures of images. In this work, we consider employing conformal mappings, which also belong to the category of diffeomorphisms. We briefly discuss three issues on this topic:

1) Transferring the alignment problem into a parameterization problem;
2) Existence of the conformal mapping;
3) Calculation of the conformal mapping.

For the sake of convenience, we assume that the involved domains or regions are simply connected on the complex plane $\mathbb{C}$, such as $D \subset \mathbb{C}$ or $\Omega \subset \mathbb{C}$. Given any two domains $\Omega_1 \subset \mathbb{C}$ and $\Omega_2 \subset \mathbb{C}$, the mapping between them can be formulated in the following way: firstly the domains are mapped onto a common region $D \subset \mathbb{C}$, hence we obtain two mappings $F_1 : D \to \Omega_1$ and $F_2 : D \to \Omega_2$, then the compound $F_2 \circ F_1^{-1} : \Omega_1 \to \Omega_2$ is the desired mapping. In this process, the common region D is set to the unit disk $D = \{w \in \mathbb{C} : |w| < 1\}$ so that it can be easily parameterized. This procedure of alignment via parameterization is visualized in Fig. 1. We restrict the mapping $F : D \to \Omega$ within the category of conformal mappings. The existence and uniqueness of the involved conformal mappings is guaranteed by the Riemann Mapping Theorem [42], [45] as follows

Theorem 1: Given any simply connected region Ω which is not the whole plane and a point $z_0 \in \Omega$, there exists a unique analytic function $f(z)$ in Ω, normalized by the conditions $f(z_0) = 0, f'(z_0) > 0$, such that $f(z)$ defines a one-to-one mapping of Ω onto the disk $D = \{w \in \mathbb{C} : |w| < 1\}$.

Although it guarantees the existence of the mapping, Theorem 1 provides no information about constructing the desired conformal mapping. Computing specific conformal mapping is a hot topic in numerical complex analysis and many studies have been made to tackle the problem [33]–[37]. In this work, we propose a novel algorithm to construct the conformal mapping. The process mainly consists of two stages: boundary corresponding and analytic extension. The main principle of this approach is to parameterize the boundary at first and then to extend the mapping into the interior area. This two stage strategy is motivated by Cauchy's integral formula, which suggests that the conformal mapping on the interior area is uniquely determined by the values on its boundary. The feasibility of this strategy is guaranteed by Theorem 2 (p235, [45])as follows

Theorem 2: If the boundary of Ω contains a free one-sided analytic arc Γ, then the mapping function has an analytic extension to $\Omega \cup \Gamma$ and Γ is mapped on an arc of the unit circle.

B. BOUNDARY CORRESPONDENCE

As is suggested in Theorem 2, firstly we need to construct an analytic arc, which can be realized via the Fourier descriptor [46], [47]. The key idea is to view the Laurent's series of the tongue boundary as a function defined on the unit circle. Suppose $w(l) = u(l) + jv(l)$, $(l = 0, 1, 2, \cdots, L-1)$ represent the points of tongue boundary $\partial \Omega$, where $j = \sqrt{-1}$. The Fourier transform of $\{w(l)\}$ is defined as follows

$$c_n = \sum_{l=0}^{L-1} w(k)e^{-j2\pi(l/L)n}, \quad (n = \pm 0, \pm 1, \pm 2, \cdots). \quad (1)$$

If we perform the inverse Fourier transform on c_n, then we can obtain the original boundary [47]. Subsequently we obtain a mapping from the unit circle $\Gamma = \{e^{j2\pi D(k/K)} | k = 0, 1, 2, \cdots, K-1\}$ to the tongue boundary. Actually, the inverse of c_n is of the formulation as follows

$$\frac{1}{L} \sum_{n=-\infty}^{\infty} c_n e^{j2\pi(k/K)n}, \quad (k = 0, 1, 2, \cdots, K-1). \quad (2)$$

Thus, we have the boundary corresponding theorem as follows

Theorem 3: Suppose the function $f(z)$ is defined as in Eq. (3), then the function $f(z)$ maps the unit circle Γ onto the region boundary $\partial \Omega$.

$$f(z) = \frac{1}{L} \sum_{n=-\infty}^{+\infty} c_n z^n, \quad (3)$$

where c_n is defined as in Eq. (1).

Proof: The points on the unit circle are of the form as follows

$$z = e^{j\theta} \quad (4)$$

or

$$z = e^{j2\pi(k/K)}. \quad (5)$$

Substituting Eq. (5) into Eq. (3), we obtain

$$f(e^{j\theta}) = f(e^{j2\pi(k/K)}) = \frac{1}{L} \sum_{n=-\infty}^{n=+\infty} c_n e^{j2(k/K)n} \quad (6)$$

The series in Eq. (6) coincides with the inverse Fourier transform Eq. (1). According to the Fourier inversion theorem, we know the function $f(e^{j2\pi(k/K)})$ maps onto the boundary $\partial \Omega$. Hence we complete the proof. ∎

Our method differs on several significant aspects from the category of Fourier series methods [34]–[36] in numerical conformal mapping. Those methods expand the desired conformal mapping into Taylor's series, where the Taylor's

coefficients is the Fourier transform of the parameterized boundary, i.e.

$$f(z) = \sum_{k=0}^{\infty} a_k z^k, \quad (7)$$

$$a_k = \frac{1}{2\pi} \int_0^{\infty} \gamma(S(\theta))e^{-jk\theta} d\theta. \quad (8)$$

The variable S here represents the arclength of the boundary. The Fourier series methods find $S = S(\theta)$ such that $f(e^{j\theta}) = \gamma(S(\theta))$ by solving a nonlinear integral equation for $S(\theta)$ by iterative algorithms [35], [36].

Our method differs from these methods on some significant aspects.

1) Firstly, rather than the Taylor's series, we use the Laurent's series as in Eq. (3). Fourier series methods map the unit *disk* onto the whole region, while our series used here only maps the unit *circle* onto the region boundary. Moreover, the Laurent's series cannot be transferred to the Taylor's series by extending the domain, since there must be a hole in the former's domain. As a result, the two approaches are essentially different.

2) Secondly, the Fourier series methods [34]–[36] need to solve a nonlinear integral equation for $S(\theta)$ by iterative algorithms. By contrast, our method needn't to solve any equation and the mapping $f(e^{j\theta})$ is straightforwardly obtained via the Fourier descriptors. Hence, our method is much more time efficient.

3) Finally, our process of boundary parameterization differs from the standard inverse Fourier transformation. Actually, the variable of the inverse Fourier transform returns to be k, hence it fails to reach the goal of parameterization. Our method further performs two variable substitution $\theta = 2\pi(k/K)$ and $z = e^{j\theta}$ so that a mapping from unit circle can be obtained.

The boundary corresponding result is visualized in Fig. 3, where the counterpart points are displayed with the same color.
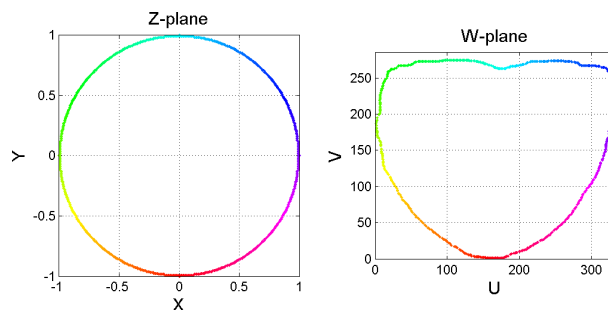

FIGURE 3. Boundary corresponding via Fourier descriptors. The counterpart points are displayed with the same color.

C. ANALYTIC EXTENSION

The construction of the conformal mapping on interior area is described in this sub-section. Both analytic and numerical

solutions are provided. The analytic solution suffers from the numerical instability near the boundaries and the numerical solution of the finite-difference method is effective to tackle the problem. Finally, we establish the convergence theorem of the proposed algorithm. Conformal mappings are well known for their nice property of smoothness. An important description of this property is Cauchy's integral formula (p119, [45]), which argues that the values on interior points are determined by the values on the boundary. Cauchy's integral formula is stated as follows

Theorem 4: Suppose that $f(z)$ is analytic in an open disk D and let Γ be a closed curve in D. For any point z_0 not on Γ,

$$f(z_0) = \frac{1}{2\pi j} \oint_{\Gamma} \frac{f(z)}{z - z_0} dz. \quad (9)$$

Cauchy's integral formula permits us to calculate the mapping on the interior area provided that the boundary correspondence is given. We discriminately denote the points on the boundary and in the interior as z and z_0 and the mappings on the boundary and on the interior area as $f(z)$ and $F(z_0)$. Hence, in the case of the curve Γ being the unit circle, Cauchy's integral formula (4) becomes

$$F(z_0) = \frac{1}{2\pi} \int_0^{2\pi} \frac{f(z)z}{z - z_0} d\theta, \quad (10)$$

where the equality holds since $z = e^{j\theta}$ and $dz = je^{j\theta} d\theta = jz d\theta$. In practical calculation, we discretized the unit circle

$$z_k = e^{j2\pi(k/K)}, \quad (11)$$

and the tongue boundary

$$\phi_k = f(z_k) = \frac{1}{L} \sum_{n=-N}^{N-1} c_n z_k^n, \quad (12)$$

then Cauchy's integral formula becomes

$$F_{p,q} = \frac{1}{K} \sum_{k=0}^{K-1} \frac{\phi_k z_k}{z_k - Z_{p,q}}, \quad (13)$$

where $F_{p,q}$ and $Z_{p,q}$ respectively represents various values of z_0 and $F(z_0)$ in Eq. (10).

However, the direct calculation using the formula Eq. (13) suffers from the difficulty of huge numerical errors, especially near the boundary, which is revealed in Fig. 4. Actually there is a difference $z - z_0$ as the denominator in Eq. (10). As the interior point z_0 approaches the boundary point z, the difference in the denominator $z - z_0$ caused huge numerical instability of $F(z_0)$. This result is not acceptable in practice, hence we need to seek resolutions to this difficulty.

D. DIFFERENCE METHODS
The finite-difference method for the Dirichlet problem is introduced to tackle the issue of boundary numerical instability. Conformal mappings are essentially complex analytic functions, the real and imaginary parts of which are conjugate harmonic functions. Suppose $F = U + j \cdot V$ is a conformal
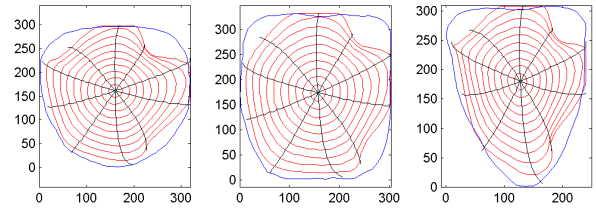

FIGURE 4. Numerical instability near the boundaries.

mapping, where U and V are real functions, then U and V are solutions of the Laplacian equations

$$\frac{\partial^2 U}{\partial x^2} + \frac{\partial^2 U}{\partial y^2} = 0, \quad (14)$$

and

$$\frac{\partial^2 V}{\partial x^2} + \frac{\partial^2 V}{\partial y^2} = 0. \quad (15)$$

Our task of analytic extension is closely related with so-called Dirichlet problems (p245, [45]), which are the first boundary problems of Laplacian equations: given its value on a closed boundary, find the solution to Laplacian equation on the interior area. In our application, we consider two related Dirichlet problems as follows:

$$\begin{cases} \dfrac{\partial^2 U}{\partial x^2} + \dfrac{\partial^2 U}{\partial y^2} = 0, \\ U|_{\Gamma} = u, \end{cases} \quad (16)$$

and

$$\begin{cases} \dfrac{\partial^2 V}{\partial x^2} + \dfrac{\partial^2 V}{\partial y^2} = 0, \\ V|_{\Gamma} = v. \end{cases} \quad (17)$$

Finite-difference methods [48] are basic numerical solutions to Dirichlet problems. For the Dirichlet problems in Eq. (16) and Eq. (17), the finite-difference methods are respectively of the iterative formats as follows:

$$\begin{aligned} U_{p,q}^{t+1} &= \frac{1}{4}(U_{p-1,q}^t + U_{p+1,q}^t + U_{p,q-1}^t + U_{p,q+1}^t) \\ V_{p,q}^{t+1} &= \frac{1}{4}(V_{p-1,q}^t + V_{p+1,q}^t + V_{p,q-1}^t + V_{p,q+1}^t) \end{aligned} \quad (18)$$

for any $(p\Delta x, q\Delta y) \in D$, and

$$\begin{aligned} U_{p,q}^{t+1} &= u_{p,q} \\ V_{p,q}^{t+1} &= v_{p,q} \end{aligned} \quad (19)$$

for any $(p\Delta x, q\Delta y) \in \Gamma$. The iterations in Eq. (18) and (19) can be used to construct the conformal mapping in question. Actually, the sequence generated via Eq. (18) and (19) respectively converges to the real and imaginary parts of the conformal mapping. We have the convergence theorem as follows,

Theorem 5: Under the conditions of

$$\begin{aligned} u(z) &= \text{Re}[f(z)], \\ v(z) &= \text{Im}[f(z)], \end{aligned} \quad (20)$$

and U^t and V^t being respectively generated by Eq. (18) and (19) where Γ is the unit circle, the sequence $\{U^t + j \cdot V^t\}$ uniformly converges to the conformal mapping Eq. (10).

Proof: Firstly, we know that the sequences U^t and V^t respectively converges to the solutions to Eq. (16) and (17). Furthermore, we know that in the case of the boundary Γ being unit circle, the solutions respectively can be expressed as Poisson's integrals. As a result, we have

$$U^t \to \frac{1}{2\pi} \int_0^{2\pi} u(z) \frac{|z|^2 - |z_0|^2}{|z - z_0|^2} d\theta \quad \text{as} \quad t \to \infty, \quad (21)$$

$$V^t \to \frac{1}{2\pi} \int_0^{2\pi} v(z) \frac{|z|^2 - |z_0|^2}{|z - z_0|^2} d\theta \quad \text{as} \quad t \to \infty, \quad (22)$$

where the integrals above are the Poisson's integrals. Under the condition of Eq. (20), we further have

$$
\begin{aligned}
U^t + j \cdot V^t &\to \frac{1}{2\pi} \int_0^{2\pi} (u(z) + j \cdot v(z)) \frac{|z|^2 - |z_0|^2}{|z - z_0|^2} d\theta \\
&= \frac{1}{2\pi} \int_0^{2\pi} f(z) \frac{|z|^2 - |z_0|^2}{|z - z_0|^2} d\theta \\
&= \frac{1}{2\pi} \int_0^{2\pi} \frac{f(z)z}{z - z_0} d\theta, \quad (23)
\end{aligned}
$$

as $t \to \infty$, where the last equality holds under the condition $z = e^{j\theta}$. Hence we completed the proof. ∎

We point out that the condition of Γ being the unit circle is crucial. Otherwise, the solutions U and V are harmonic but not necessarily conjugate to each other. As a result, the mapping $U + j \cdot V$ is not necessarily conformal.

E. MAPPING IMPLEMENTATION

In this subsection, we describe the mapping implementation process after the mapping function has been obtained. We discuss two categories of mappings as follows

1) Mapping a tongue region Ω_1 onto the disk D;
2) Mapping a tongue region Ω_1 onto another tongue region Ω_2.

1) MAPPING A TONGUE ONTO THE DISK

Suppose the original and aligned images are respectively denoted as $I_1[u, v, w]$ and $J[x, y, w]$, where $(u, v) \in \Omega_1$ (tongue domain), $(x, y) \in D$ (disk), and $w = 1, 2, 3$ (three channels of RGB), then the aligned image can be expressed in the term of the original image as follows:

$$J[x, y, w] = I_1[U(x, y), V(x, y), w] \quad (24)$$

for each $(x, y) \in D$ and $w = 1, 2, 3$. Notice that the computation is performed on each fixed pixel (x, y) respectively and the variables $U(x, y)$ and $V(x, y)$ are numbers rather than matrices, hence they can serve as subscripts/coordinates in Eq. (24).

The process of mapping any given tongue image on to the disk is described in Table 1.

TABLE 1. Proposed alignment algorithm: Mapping a tongue region onto the disk.

Input the original image $I_0[u, v, w]$ and its domain $\Omega \subset \mathbb{C}$
Step 1. Compute the region boundary $\{w_l\}_{l=1}^L$ and its Fourier coefficient $\{c_n\}_{n=-N}^{N-1}$ via Eq. (1).
Step 2. Compute the boundary correspondence $\phi_k = f(z_k)$ via Eq. (12).
Step 3. Compute the initial mapping F via Eq. (13), and set $U = \text{Re}[F]$ and $V = \text{Im}[F]$.
Step 4. Update U and V iteratively via Eq. (18)-(19) until the termination condition is satisfied.
Output the mapping $F = U + j \cdot V$ and the aligned image $I_1[x, y, w]$ via Eq. (24).

2) MAPPING BETWEEN TONGUES

The compound mappings between any given moving and fixed images is visualized in Fig. 1 and is described as follows.

Suppose the moving and fixed images are respectively denoted as $I_1[u, v, w]$ and $I_2[\tilde{u}, \tilde{v}, w]$, where $(u, v) \in \Omega_1$ and $(\tilde{u}, \tilde{v}) \in \Omega_2$. The mappings $F_1 : \Omega_1 \to D$ and $F_2 : \Omega_2 \to D$ can be obtained via the approach described in Table 1.

Respectively denote the forms of F_1 and F_2 as $F_1 = U + j \cdot V$ and $F_2 = \tilde{U} + j \cdot \tilde{V}$. Notice that the mapping $(\tilde{U}(x, y), \tilde{V}(x, y))$ is a one-to-one mapping. Hence, for each $(\tilde{u}, \tilde{v}) \in \Omega_2$, denote the corresponding pixel in the disk as $(X(\tilde{u}, \tilde{v}), Y(\tilde{u}, \tilde{v})) \in D$. Thus, the aligned image from the disk to Ω_2 can be expressed as

$$I_2[\tilde{u}, \tilde{v}, w] = J[X(\tilde{u}, \tilde{v}), Y(\tilde{u}, \tilde{v}), w] \quad (25)$$

for each $(\tilde{u}, \tilde{v}) \in \Omega_2$ and $w = 1, 2, 3$.

As is discussed in Section III-E.1, the aligned image onto the disk can be obtained via Eq. (24). Substituting Eq. (24) into Eq. (25), we obtain

$$I_2[\tilde{u}, \tilde{v}, w] = I_1[U(X(\tilde{u}, \tilde{v}), Y(\tilde{u}, \tilde{v})), V(X(\tilde{u}, \tilde{v}), Y(\tilde{u}, \tilde{v})), w]. \quad (26)$$

Thus, we obtain the aligned image from I_1 to I_2.

Notice in Eq. (26) that the intensity information of the fixed image I_2 is not necessary. Actually, it can be obtained via the original image I_1, as Eq. (26) indicates. In the practice of alignment, only the shape of the fixed image is needed. This fact is crucial to the choice of a fixed image in our experiments, as is discussed in Section IV-A and V-B.

IV. APPLICATION

The conformal alignment method is applied to feature extraction in this section. The constructions of average tongues and eigen-tongues are presented and the classical PCA [49] is introduced to dimensionality reduction.

A. CHOICE OF FIXED SHAPES

In our application the intensity of the fixed image is not necessary, since the alignment results only depend on the shape of the fixed image. Hence, we discriminately use the terminology of the *fixed shape* and the *fixed image*, where the former only refers to the form of the tongue area and the latter additionally includes the intensity information.
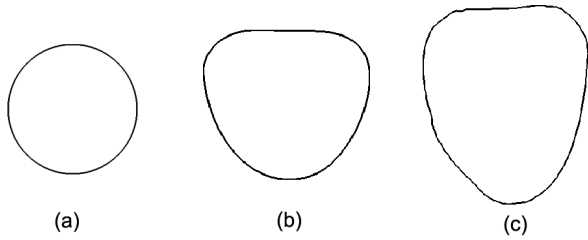
FIGURE 5. Various fixed shapes used in this work: (a) the disk with 64-pixel radius; (b) the average shape of the tongue; (c) the shape of a randomly chosen tongue image.

The computations of average tongues, eigen-tongues, and feature extraction involve two fixed shapes. In Section V-D, the shape of a real tongue image is used as the fixed shape. The involved fixed shapes are displayed in Fig. 5. For the sake of clarity, we only display the boundaries of the related domains/shapes.

In the application of feature extraction, the fixed shape is the disk with a 64-pixel radius (briefly denoted as 64-disk), which is shown in Fig. 5-a. This methodology is based on the time consuming consideration. Actually, we only need to perform the process in Table (1) without the mapping in Eq. (26), which is more economical from a timing respective on large-scale databases.

For the presentation of the average tongues and eigen-tongues, we use as the fixed shape a so-called average shape of the tongues (briefly referred as average shape), which is displayed in Fig. 5-b. This is for the sake of a more intuitive presentation, since the average shape "aligns" with our intuition on tongue shape more than the disk does.

The computation of the average shape is performed as follows: an average Fourier descriptor is computed by averaging the Fourier descriptors of all the tongue images at each component, before the average shape of the tongue is obtained by calculating the inverse Fourier transformation of the average Fourier descriptor.

In Section V-D, we employ as the fixed shape the domain of a randomly chosen tongue image, which is shown in Fig. 5-c. In this specific experiment, we need to employ the intensity value of the fixed image as the ground-truth, based on which the alignment performance of other images can be evaluated. For this reason, the fixed shape must be the domain of a real tongue image. Hence, we randomly chose a tongue image as the fixed image, the domain of which is used as the fixed shape.

B. AVERAGE TONGUES

We propose the concept of average tongue, which presents the common tongue features of a disease in a single tongue image. The average tongues are formulated via the processes as follows:

1) All the tongue images are aligned onto the average shape, as is demonstrated in Fig. 1;
2) Within each class, the average color at each pixel of the average shape is calculated;
3) The pixel-wise average image is the average tongue.

Readers are reminded of the difference between the concepts of *average shape* and *average tongue*, where the former only refers to a specific area as shown in Fig. 5 and the later includes color information on the average shape.

We perform the process on a tongue image dataset of 3,980 images, which contains eleven classes. More detailed information is provided in Section V-A. The average tongues of some classes are showcased in Fig. 6. For the sake of placement, we only displayed the average tongues of eight classes, where the color has been enhanced via histogram equalization for better observation. Fig. 6 reflects some interesting phenomenon which agrees with some basic observations in practical tongue diagnosis. The healthy tongue appears light reddish and smooth, and is partially covered with light yellow coating. On the contrary, the tongues of disease classes appears very differently. For example, the Diabetes tongue is in purplish and the Lung Cancer tongue is dark and coarse, covered with a thick and yellow coating. The crack marks on the coating are also evident. These observations verify some empirical rules in tongue diagnosis.

C. FEATURE EXTRACTION AND EIGEN-TONGUES

Theoretically speaking, the aligned tongue images can be directly used as feature vectors; however we prefer to reduce the dimensionality via the principle component analysis (PCA) to reduce the computation cost.

Suppose the n-th underlying images in the dataset is denoted as $\mathcal{I}_n[u, v, w]$ ($n = 1, \cdots, N$ and $w = 1, \cdots, c$), then the procedure in Table 2 describes feature extraction from $\mathcal{I}_n[u, v, w]$ via PCA. We declare that the underlying images $\mathcal{I}_n[u, v, w]$ are not necessarily the original RGB images and can be some processed images.

TABLE 2. Feature extraction via PCA.

Input the underlying images $\mathcal{I}_n[u, v, w]$ ($n=1,\cdots,N$).
Step 1. Align $\mathcal{I}_n[u, v, w]$ onto the 64-disk domain via the procedure in Table 1; The aligned images are denoted as $\mathcal{J}_n[x, y, w]$ ($x, y=1,\cdots,128$);
Step 2. Vectorize the tongue region of the aligned images $\mathcal{J}_n[x, y, w]$ into the s-dimensional vectors $\boldsymbol{x}_n \in \mathbb{R}^s$ where $s=12,868\approx\pi 64^2$; All the column vectors $\boldsymbol{x}_n$ form the data matrix $\boldsymbol{X} = [\boldsymbol{x}_1, \cdots, \boldsymbol{x}_N]$;
Step 3. Given an integer $d<s$, find the first d eigenvectors $\boldsymbol{w}_n \in \mathbb{R}^s$ ($n=1,\cdots,d$) of the covariance matrix $\boldsymbol{X}\boldsymbol{L}\boldsymbol{X}^{\mathrm{T}}$, where $\boldsymbol{L}=\frac{1}{s}\boldsymbol{I} - \frac{1}{s^2}\boldsymbol{e}\boldsymbol{e}^T$. The first d eigenvectors form the projection matrix $\boldsymbol{W} = [\boldsymbol{w}_1, \cdots, \boldsymbol{w}_d]$;
Step 4. The feature vector $\boldsymbol{y}_n \in \mathbb{R}^d$ of the n-th sample is obtained via $\boldsymbol{y}_n = \boldsymbol{W}^{\mathrm{T}}\boldsymbol{x}_n$.
Output the feature vector $\boldsymbol{y}_n \in \mathbb{R}^d$.

1) COLOR FEATURE EXTRACTION

In the extraction of color features, the underlying image is just the original RGB image, i.e., $\mathcal{I}_n[u, v, w] = I_n[u, v, w]$ and $c = 3$.

Reshaping the n-th eigenvector $\boldsymbol{w}_n \in \mathbb{R}^s$ into a 64-disk region, where the process is the inversion of transforming the 64-disk into s-dimensional vectors, we can obtain the n-th eigen-image.

To present the eigen-images in an intuitional form, the disk-formed eigen-images are aligned to the average shape and the aligned eigen-images are called eigen-tongues,
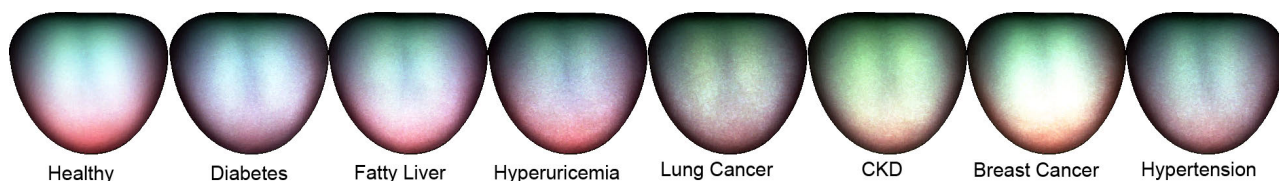
FIGURE 6. Average tongues of some disease (or healthy population). The images are generated on real tongue images.

Healthy | Diabetes | Fatty Liver | Hyperuricemia | Lung Cancer | CKD | Breast Cancer | Hypertension
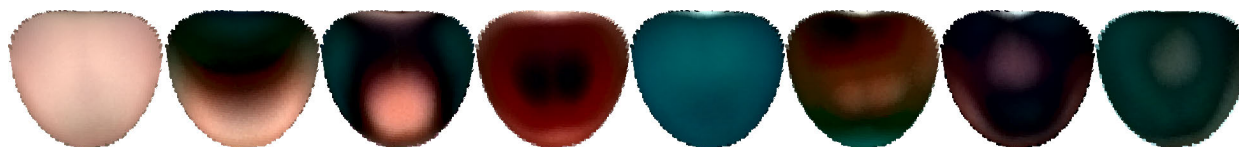

FIGURE 7. The first eight eigen-tongues obtained on the database. Some vague partition boundaries can be seen in the eigen-tongues.

the terminology of which is analogous to the notation of eigenface in face recognition [18].

The first eight eigen-tongues of our database are displayed in Fig. 7[2]. The eigen-tongues are naturally partitioned by their appearances, which suggest some functional sectorizatoin information on tongue surface. Notice that this partition is data-driven, despite the fact that the existing partition schemes are defined by humans.

2) TEXTURE FEATURE EXTRACTION

In the extraction of texture features, a similar procedure in Table 2 is performed. The only difference is that the underlying image becomes the Gabor filter response, which is obtained via the methodology in [10].

Suppose $\{G[x, y, \sigma_i, \theta_j]\}(i = 1, \cdots, 3$ and $j = 1, \cdots, 4)$ is a bank of Gabor filters as follows

$$G[x, y, \sigma_i, \theta_j] = \frac{1}{2\pi\sigma_i^2} \exp\left(\frac{x'^2 + \gamma^2 y'^2}{-2\sigma_i^2}\right) \exp\left(\frac{2\pi j x'}{\sigma_i}\right),$$

$$(27)$$

where $x' = x\cos\theta_j + y\sin\theta_j$, $y' = -x\sin\theta_j + y\cos\theta_j$, σ_i is the variance, γ the aspect ratio of the sinusoidal function, and θ_j the orientation. A total of three σ_i (1, 2, and 3) and four θ_j (0°, 45°, 90°, and 135°) choices are used.

The extraction of texture feature is performed as follows

1) Convert the original RGB image $I_n[x, y, w]$ into a gray image $I_n[x, y]$;
2) Compute the maximal Gabor response $\mathcal{I}[x, y]$ via

$$\mathcal{I}[x, y] = \max_{i,j} G[x, y, \sigma_i, \theta_j] * I[x, y]; \quad (28)$$

3) View $\mathcal{I}[x, y]$ as the the underlying image and process $\mathcal{I}[x, y]$ via the procedure described in Table 2.

Thus, we obtain the feature vector of the Gabor filter texture.

[2]The negative components of eigen-tongues are displayed in color opponents. For example, the negative components in the red channel are displayed in crayon. The coarseness of the edges of the eigen-tongues are caused by this fact: The images are first downsampled to reduce the computation cost of the eigenvalue problem in PCA, before the obtained eigenvector is upsampled to the original size and mapped to the average shape.
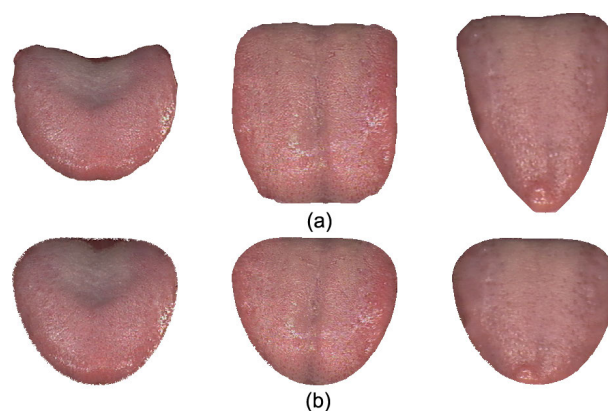

FIGURE 8. Alignment results on samples of various shapes. The original images (a) are of various shapes, respectively round, quadrate, and triquetrous. The aligned images (b) are adapted harmonically to the fixed shape.

V. EXPERIMENTS

A. IMAGE ACQUISITION AND DATABASE

The experiments in this work are performed on a tongue image database consisting of 3,980 images, each of which exclusively corresponds to an individual. The images are obtained via a specially designed device, which in appearance is mainly a closed box with a capture window. The box contains a controlled imaging environment including a 3-CCD camera lens. The subject shows his/her tongue through the window to the lens. The imaging is processed on an embedded system in the device and can be controlled by an external personal computer.

The captured images are stored in the standard BMP format, where 8×3 (3 channels) bits are employed to represent a color pixel. Afterwards, the image color is calibrated for an accurate description. Finally, the tongue body is specially segmented from the background. An example of the calibrated and segmented image can be found in Fig. 1 — the moving image. (In the later sections, more examples can be found in Fig. 8-a, 9-b, and 11.) The detailed information about the
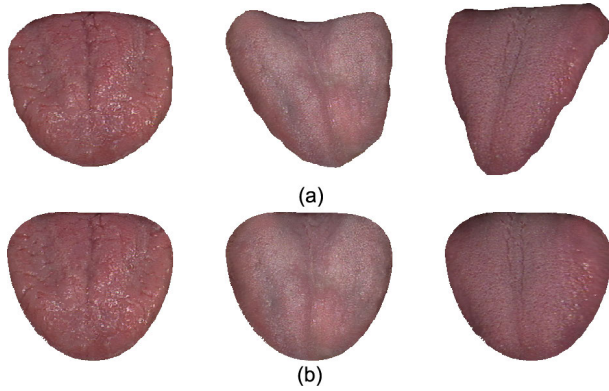
FIGURE 9. Alignment results on samples of various orientations. The original tongue tips (a) are respectively vertical, skewed to left, and skewed to right. The registered tongue tips and cracks (b) are all well-aligned vertically.

TABLE 3. Classes of the dataset and their sample numbers.

Class	Sample Number
Healthy	1,227
Diabetes	485
Fatty Liver	368
Abnormal Lipid Metabolism (ALM)	326
Hyperlipidemia	274
Chronic Kidney Disease (CKD)	268
Breast Cancer	265
Hypertension	259
Bradycardia	219
Hyperuricemia	196
Lung Cancer	193

imaging device and color calibration can be found in [50] and the segmentation method in [22].

The segmented images are on average 280×283 in size. The database contains 11 classes, the names and sample numbers of which are listed in Table 3.

B. CHOICE OF FIXED SHAPES AND MOVING IMAGES

In this subsection, we relate the choice of the fixed and moving images in the experiments. The choice of the fixed shape varies according to different goals. In the experiments we aim for three goals, of which the fixed and moving images are chosen as follows

1) ALIGNMENT RESULT PRESENTATION

The alignment results are demonstrated on six images of various shapes and orientations, which are displayed in Fig. 8-a and 9-a. These images are used as the moving images, and the average shape shown in Fig. 5-c as the fixed shape.

2) ALIGNMENT ACCURACY EVALUATION

The registration is performed on the four images, which are captured from an identical individual. We randomly chose one image as the fixed image and the remaining three images as the moving images. Notice that these images are not included in the set of the aforementioned 3,980 images, in which one individual only has one image.

3) FEATURE EXTRACTION

For the application of feature extraction and disease detection, the 64-disk shown in Fig. 5-a is chosen as the fixed shape and the 3,980 images in the database are the moving images.

C. ALIGNMENT RESULTS

In this subsection, we display the alignment results on some samples of various shapes and show that with the aid of the proposed method, the existing region partition methods performed on rigid body can be adaptively corrected.

A MatLab program of the conformal mapping computation has been uploaded to `https://codeocean.com/capsule/4382908/tree/v1`, where the program, named as "Tongue Conformal Mappings", is publicly accessible and can be utilized in other applications by interested researchers. The experimental results in this subsection can be reproduced via the program.

1) ALIGNMENT ONTO THE AVERAGE SHAPE

Fig. 8 and Fig. 9 showcase the alignments of several samples onto the average shape. Fig. 8-a and Fig. 9-a are the original images and Fig. 8-b and Fig. 9-b the corresponding alignment results.

The original tongues in Fig. 8-a show various shapes, respectively round, quadrate, and triquetrous. While the alignments in Fig. 8-b show that all the tongues are adapted harmonically to the fixed shape.

Fig. 9 demonstrates the robustness of the proposed method against various tongue orientations. The tongue tips in Fig. 9-a orient to various directions, where the first tongue is vertical and the rest tongues are skewed to respectively left and right. In the alignment results of Fig. 9-b, all the tongues are well adapted vertically. Especially all the central main cracks are vertical in the aligned images, despite of the fact that some of them originally oriented to different directions in the moving images.

2) REGION PARTITION CORRECTION

The proposed method can be applied to correct region partition adaptively. The existing region partition approaches usually assume the underlying tongues are vertical. Hence, the partition results can be misplaced when the underlying tongue shape violates the assumption. The partition results of the method in [6] are shown in Fig. 10-a, where the areas of the edge regions on the left and right sides are severely imbalanced.

To tackle the malposition issue, we suggest to correct the partition as follows: firstly perform the partition on the aligned image via the proposed method, which is shown in Fig. 10-b; then obtain the partition on the original image via the inverse alignment mapping, as is shown in Fig. 10-c. The issue of edge region imbalance is remarkably reduced on the corrected partition results. Moreover, the corrected region boundaries curves according to the tongue deformations.
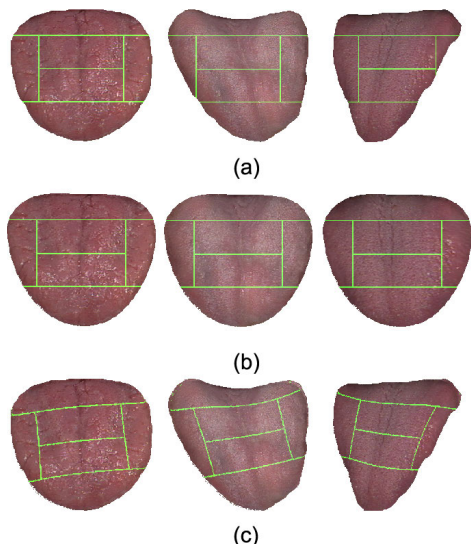
FIGURE 10. The proposed alignment method helps to partition the tongue regions adaptively. (a) Original partition proposed in [6]; (b) Partition on the aligned images; (c) Corrected partition on the original images via the inverse of the alignment mapping.

FIGURE 11. The moving and fixed images in the alignment accuracy evaluation. The first three images are used moving images and the last as the fixed image. All the images are captured from an identical tongue body; hence, the tongue colors are generally coherent with one another.

D. ALIGNMENT ACCURACY EVALUATION

We compared the alignment accuracy, conformality, and CPU time of the proposed method with some existing conformal mappings, which includes

1) Schwarz-Christoffel Mapping (SC) [37];
2) Numerical conformal mapping software: Zipper [51];
3) Geometric Processing Package (GPP) [52];
4) Fast Disk Conformal Map (FDM) [53];
5) Conformal Energy Minimization (CEM) [54].

The first two methods belong to the category of 2d conformal mappings—mappings between 2d complex planes, while the last three methods are 3d conformal mappings—mappings between plane and 3d surface. For the 3d conformal mappings, the image is firstly meshed via the triangulation procedure and then the 3d conformal mappings are performed on the meshed plane. All programs are written in Matlab scripts and are run on a PC platform with a two core Intel CPU of 3.40 GHz and 3.70 GHz.

Following the methodology in [55], [56], we employ as the registration criteria the sum of squared differences (SSD),

which is defined as follows

$$\text{SSD} = \sum_{i,j} \left[(L_{i,j} - L^*_{i,j})^2 + (a_{i,j} - a^*_{i,j})^2 + (b_{i,j} - b^*_{i,j})^2 \right], \tag{29}$$

where $(L_{i,j}, a_{i,j}, b_{i,j})$ and $(L^*_{i,j}, a^*_{i,j}, b^*_{i,j})$ respectively represents the CIE-Lab values of the aligned and the fixed image at the pixel (i, j). Notice that each term of the sum in Eq. (29) is just the color error at the pixel (i, j):

$$\text{ColErr}(i, j) = (L_{i,j} - L^*_{i,j})^2 + (a_{i,j} - a^*_{i,j})^2 + (b_{i,j} - b^*_{i,j})^2. \tag{30}$$

Besides the SSD, we also use as the measurement of the conformality of the mappings Cauchy-Riemann error (C-R error), which defined as follows

$$\text{C-R Error} = \max_{(x,y) \in D} \left\{ \frac{\partial U}{\partial x} - \frac{\partial V}{\partial y}, \frac{\partial V}{\partial x} + \frac{\partial U}{\partial y} \right\}. \tag{31}$$

For the iterations of the proposed method, the stopping condition is set as follows

$$\frac{|\text{error}^t - \text{error}^{t-1}|}{|\text{error}^{t-1}|} \leq 10^{-4}, \tag{32}$$

where error^t is the C-R error defined in Eq. (31).

The registration results and the color errors of the first moving image are displayed in Fig. 12, where the upper row contains the first moving image, the fixed image, and the aligned images via the compared mappings. The lower row corresponds to the color errors between the aligned images and the fixed image. The errors are displayed in the index images using the colormap of *hot*.

The numerical comparison of the C-R errors, SSD and CPU times are shown in Table 4. The SSD of the SC mapping is missing and represented by a bar in Table 4, since the SC mapping fails to map the tongue images to the unit disk, which denies the feasibility of accurate registration. The methods of GPP and CEM are the fastest of all the compared methods, actually the CPU times of both are about 1.0 second. The proposed method is slightly slower, costing about 5.5 seconds and the remaining methods are much slower. From this viewpoint, the proposed method is not the most efficient but sub-optimal. On the other hand, as is shown in Table 4 the C-R error of the proposed method is less 10 pixels, while those of the baseline methods are all above 290 pixels. Moreover, the SSD of the proposed method is also the minimum of all the compared approaches. Hence, from the viewpoint of alignment accuracy and comformality, the proposed method is more accurate than any other baseline method.

TABLE 4. Cauchy-Riemann error, sum of squared difference (e+05) and CPU time (s) of compared methods.

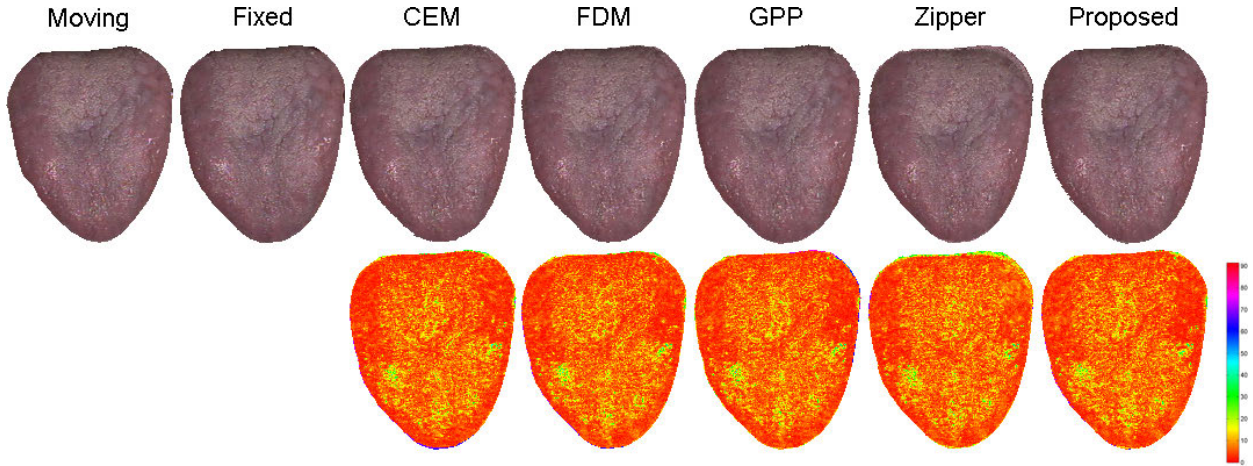|	SC	Zipper	CEM	FDM	GPP	Proposed
SSD	—	5.49	4.91	4.93	4.81	**4.66**
C-R Error	268.00	274.83	291.00	289.50	289.33	**8.83**
Time	95.27	207.33	1.03	13.57	**0.84**	5.53

FIGURE 12. Upper row: moving, fixed, and registered images via compared mappings. Lower row: registered errors (in pixel-wise CIE-Lab difference).

E. DISEASE DETECTION

The proposed features are compared with the following existing features for disease detection.

1) CTES [1] (10 dimensional color, 7 dimensional texture);
2) CATDS [5] (110 dimensional color, 10 dimensional texture);
3) Gamut (12 dimensional). Tongue color feature firstly proposed in [9], is the main tool used in [10].
4) Gabor (9 dimensional). Tongue texture feature proposed in [10]. It is mainly based on maximal Gabor response.

We performed a set of classifications of healthy vs. a disease. All diseases are randomly split into five equal sessions. One session is used as the testing set and the others as the training set.

The classic supporting vector machine (SVM) [57] is used as the classifier. The parameter box constraint is defined as C in this paper. We run the value of C through a discrete set of {0.005, 0.01, 0.05, 0.1, 0.5, 1} and record the best performance. The feature set is also optimized via the sequential forward selection [58], where the wrapper is the SVM. The optimal dimensionality choice is studied at first. All images are aligned to a disk domain of $R = 64$ and then down-sampled with the sampling factor of 2. The dimensions of the resulting texture feature and color feature are respectively 3,209 and 9,627 (3 channels). They are respectively reduced to 110 dimensions, since the dimensions of the baseline features vary from 10 to 110. The optimal accuracies of the compared color features are displayed in Table 5 and the results of the textures in Table 6. Every row in the tables corresponds to a disease detection problem and the maximum accuracy is displayed in bold. For a more detailed awareness of the classification results, the confusion matrices of the proposed method detecting the first three diseases with color

TABLE 5. Detection accuracies (%) of color features.

Disease	Gamut	CTES	CATDS	ConfMap+PCA
Diabetes	62.89	74.74	77.32	**86.60**
Fatty Liver	58.78	74.32	75.68	**80.41**
ALM	56.92	70.00	71.54	**80.00**
Hyperlipidemia	50.91	77.27	**87.27**	77.27
CKD	54.63	67.59	81.48	**87.96**
Breast Cancer	53.77	78.30	73.58	**86.79**
Hypertension	52.88	75.96	79.81	**90.38**
Bradycardia	56.82	77.27	79.55	**81.82**
Hyperuricemia	67.95	78.21	**88.46**	85.90
Lung Cancer	57.69	74.36	79.49	**93.59**
Average	57.32	74.80	79.42	**85.07**

TABLE 6. Detection accuracies (%) of texture features.

Disease	Gabor	CTES	CATDS	ConfMap+PCA
Diabetes	61.34	55.15	68.56	**82.99**
Fatty Liver	66.22	62.16	60.14	**71.62**
ALM	64.62	59.23	60.77	**70.00**
Hyperlipidemia	65.45	62.73	60.00	**78.18**
CKD	68.52	63.89	62.96	**78.70**
Breast Cancer	65.09	56.60	71.70	**83.96**
Hypertension	61.54	55.77	66.35	**74.04**
Bradycardia	67.05	57.95	69.32	**78.41**
Hyperuricemia	74.36	62.82	75.64	**85.90**
Lung Cancer	71.79	70.51	74.36	**82.05**
Average	66.60	60.68	66.98	**78.59**

TABLE 7. Confusion matrix of diabetes detection (in sample number).

	Predict Healthy	Predict Diabetes
True Healthy	88	9
True Diabetes	17	80

features (corresponding to the first three rows in Table 5) are respectively displayed in Tables 7, 8, and 9.

The result in Table 5 shows that in general, the proposed color feature (denoted as ConfMap+PCA) outperforms the other baseline features. In fact, the average accuracy of ConfMap+PCA is 85.07%, higher than the other features by

TABLE 8. Confusion matrix of fatty liver detection (in sample number).

	Predict Healthy	Predict Fatty Liver
True Healthy	60	14
True Fatty Liver	15	59

TABLE 9. Confusion matrix of ALM detection (in sample number).

	Predict Healthy	Predict ALM
True Healthy	50	15
True ALM	11	54

about 5.65%. Except for Hyperlipidemia and Hyperuricemia detections, the proposed feature performs better than the others. In the cases of Hyperlipidemia and Hyperuricemia detections, the optimal feature is CATDS, which outperforms ConfMap+PCA respectively by 10% and 2.56%. In the other cases, the accuracy of the proposed feature is higher than the baseline features by about ten percent. Especially on the cases of Diabetes and Lung Cancer, the improvements are respectively up to 10.58% and 14.10%. The texture feature results in Table 6 are generally poorer than the color features. Nevertheless, the proposed texture feature achieves maximum accuracies in all the disease detections. The accuracies of the proposed feature are about 78.59%, which is approximately 11.61% higher than the other texture features. These results reveals that the PCA features based on conformal alignment can effectively improve the performance of disease detection.

VI. CONCLUSION

In this paper, we proposed an image alignment method by conformal mapping. The conformal mapping is obtained via a two stage algorithm. The mapping on the boundary is firstly determined and then is extended onto its interior. The computation cost is remarkably reduced via transfering the computation load from the interior to the boundary. The numerical comparison verifies that the accuracy of the proposed algorithm is much better than several popular conformal mapping tools. The conformal alignment method is also applied to construct eigen-tongues and PCA features, which improves the disease detection performance. These experiments suggest that the proposed method provides an accurate and efficient tool for image alignment and feature extraction.

REFERENCES

[1] C.-C. Chiu, "A novel approach based on computerized image analysis for traditional Chinese medical diagnosis of the tongue," *Comput. Methods Programs Biomed.*, vol. 61, no. 2, pp. 77–89, 2000.

[2] C. H. Li and P. C. Yuen, "Tongue image matching using color content," *Pattern Recognit.*, vol. 35, no. 2, pp. 407–419, 2002.

[3] B. Pang, D. Zhang, N. Li, and K. Wang, "Computerized tongue diagnosis based on Bayesian networks," *IEEE Trans. Biomed. Eng.*, vol. 51, no. 10, pp. 1803–1810, Oct. 2004.

[4] H. Z. Zhang, K. Q. Wang, D. Zhang, B. Pang, and B. Huang, "Computer aided tongue diagnosis system," in *Proc. 27th Annu. Conf. IEEE Eng. Med. Biol.*, Jan. 2006, pp. 6754–6757.

[5] B. Pang, D. Zhang, and K. Wang, "Tongue image analysis for appendicitis diagnosis," *Inf. Sci.*, vol. 175, no. 3, pp. 160–176, 2005.

[6] Y.-G. Wang, J. Yang, Y. Zhou, and Y.-Z. Wang, "Region partition and feature matching based color recognition of tongue image," *Pattern Recognit. Lett.*, vol. 28, no. 1, pp. 11–19, 2007.

[7] X. Wang and D. Zhang, "An optimized tongue image color correction scheme," *IEEE Trans. Inf. Technol. Biomed.*, vol. 14, no. 6, pp. 1355–1364, Nov. 2010.

[8] J. Kim, G. J. Han, and B. H. Choi, "Development of differential criteria on tongue coating thickness in tongue diagnosis," *Complementary Therapies Med.*, vol. 20, no. 5, pp. 316–322, 2012.

[9] X. Wang, B. Zhang, Z. Yang, H. Wang, and D. Zhang, "Statistical analysis of tongue images for feature extraction and diagnostics," *IEEE Trans. Image Process.*, vol. 22, no. 7, pp. 5336–5347, Dec. 2013.

[10] B. Zhang, B. V. K. V. Kumar, and D. Zhang, "Detecting diabetes mellitus and nonproliferative diabetic retinopathy using tongue color, texture, and geometry features," *IEEE Trans. Biomed. Eng.*, vol. 61, no. 2, pp. 491–501, Feb. 2014.

[11] M. Kainuma, N. Furusyo, Y. Urita, M. Nagata, T. Ihara, T. Oji, T. Nakaguchi, T. Namiki, and J. Hayashi, "The association between objective tongue color and endoscopic findings: Results from the Kyushu and Okinawa population study (KOPS)," *BMC Complementary Alternative Med.*, vol. 15, no. 1, p. 372, 2015.

[12] Y. Cui, S. Liao, H. Wang, H. Liu, W. Wang, and L. Yin, "Relationship between hyperuricemia and Haar-like features on tongue images," *Biomed. Res. Int.*, vol. 2015, Dec. 2014, Art. no. 363216.

[13] P.-C. Hsu, Y.-C. Huang, J. Y. Chiang, H.-H. Chang, P.-Y. Liao, and L.-C. Lo, "The association between arterial stiffness and tongue manifestations of blood stasis in patients with type 2 diabetes," *BMC Complementary Alternative Med.*, vol. 16, no. 1, p. 324, 2016.

[14] J. Li, D. Zhang, Y. Li, and J. Wu, "Multi-modal fusion for diabetes mellitus and impaired glucose regulation detection," 2016, *arXiv:1604.03443*. [Online]. Available: https://arxiv.org/abs/1604.03443

[15] L. G. Brown, "A survey of image registration techniques," *ACM Comput. Surv.*, vol. 24, no. 4, pp. 325–376, Dec. 1992.

[16] B. Zitová and J. Flusser, "Image registration methods: A survey," *Image Vis. Comput.*, vol. 21, pp. 977–1000, Oct. 2003.

[17] J. Wright, A. Y. Yang, A. Ganesh, S. S. Sastry, and Y. Ma, "Robust face recognition via sparse representation," *IEEE Trans. Pattern Anal. Mach. Intell.*, vol. 31, no. 2, pp. 210–227, Feb. 2009.

[18] M. A. Turk and P. Alex Pentland, "Face recognition using eigenfaces," in *Proc. Comput. Soc. Conf. Comput. Vis. Pattern Recognit.*, Jun. 1991, pp. 586–591.

[19] P. N. Belhumeur, J. P. Hespanha, and D. J. Kriegman, "Eigenfaces vs. Fisherfaces: Recognition using class specific linear projection," *IEEE Trans. Pattern Anal. Mach. Intell.*, vol. 19, no. 7, pp. 711–720, Jul. 1997.

[20] X. He, S. Yan, and Y. Hu, "Face recognition using Laplacianfaces," *IEEE Trans. Pattern Anal. Mach. Intell.*, vol. 27, no. 3, pp. 328–340, Mar. 2005.

[21] B. Huang, J. Wu, and D. Zhang, "Tongue shape classification by geometric features," *Inf. Sci.*, vol. 180, no. 2, pp. 312–324, 2010.

[22] K. Wu and D. Zhang, "Robust tongue segmentation by fusing region-based and edge-based approaches," *Expert Syst. Appl.*, vol. 42, no. 21, pp. 8027–8038, Nov. 2015.

[23] T. Brox, A. Bruhn, and N. Papenberg, "High accuracy optical flow estimation based on a theory for warping," in *Proc. Eur. Conf. Comput. Vis.* Berlin, Germany: Springer, 2004, pp. 25–36.

[24] C. Liu, J. Yuen, and A. Torralba, "SIFT flow: Dense correspondence across scenes and its applications," *IEEE Trans. Pattern Anal. Mach. Intell.*, vol. 33, no. 5, pp. 978–994, May 2011.

[25] Z. Chen, H. Jin, and Z. Lin, "Large displacement optical flow from nearest neighbor fields," in *Proc. IEEE Conf. Comput. Vis. Pattern Recognit.*, Jun. 2013, pp. 2443–2450.

[26] M. F. Beg, M. I. Miller, A. Trouvé, and L. Younes, "Computing large deformation metric mappings via geodesic flows of diffeomorphisms," *Int. J. Comput. Vis.*, vol. 61, no. 2, pp. 139–157, 2005.

[27] J. Ashburner, "A fast diffeomorphic image registration algorithm," *NeuroImage*, vol. 38, no. 1, pp. 95–113, 2007.

[28] B. B. Avants, C. L. Epstein, M. Grossman, and J. C. Gee, "Symmetric diffeomorphic image registration with cross-correlation: Evaluating automated labeling of elderly and neurodegenerative brain," *Med. Image Anal.*, vol. 12, no. 1, pp. 26–41, 2008.

[29] B. D. de Vos, F. F. Berendsen, and M. A. Viergever, "End-to-end unsupervised deformable image registration with a convolutional neural network," in *Deep Learning in Medical Image Analysis and Multimodal Learning for Clinical Decision Support.* Cham, Switzerland: Springer, 2017, pp. 204–212.

[30] H. Li and Y. Fan, "Non-rigid image registration using fully convolutional networks with deep self-supervision," 2017, *arXiv:1709.00799*. [Online]. Available: https://arxiv.org/abs/1709.00799

[31] G. Balakrishnan, A. Zhao, M. R. Sabuncu, J. Guttag, and A. V. Dalca, "An unsupervised learning model for deformable medical image registration," in *Proc. IEEE Conf. Comput. Vis. Pattern Recognit.*, Jun. 2018, pp. 9252–9260.

[32] C. Tian, Y. Xu, and W. Zuo, "Image denoising using deep CNN with batch renormalization," *Neural Netw.*, vol. 121, pp. 461–473, Jan. 2020.

[33] D. Gaier, "Ermittlung des konformen moduls von vierecken mit differenzenmethoden," *NumerischeMath.*, vol. 19, no. 2, pp. 179–194, 1972.

[34] P. Henrici, "Fast Fourier methods in computational complex analysis," *SIAM Rev.*, vol. 21, no. 4, pp. 481–527, 1979.

[35] B. Fornberg, "A numerical method for conformal mappings," *SIAM J. Sci. Stat. Comput.*, vol. 1, no. 3, pp. 386–400, 1980.

[36] R. Wegmann, "Convergence proofs and error estimates for an iterative method for conformal mapping," *Numerische Mathematik*, vol. 44, no. 3, pp. 435–461, 1984.

[37] T. A. Driscoll and L. N. Trefethen, *Schwarz-Christoffel Mapping*. Cambridge, U.K.: Cambridge Univ. Press, 2002.

[38] D. Zhang and M. Hebert, "Harmonic maps and their applications in surface matching," in *Proc. Comput. Soc. Conf. Comput. Vis. Pattern Recognit.*, vol. 2, Jun. 1999, pp. 524–530.

[39] Y. Wang, X. Gu, T. F. Chan, P. M. Thompson, and S.-T. Yau, "Intrinsic brain surface conformal mapping using a variational method," *Proc. SPIE*, vol. 5370, pp. 241–252, May 2004.

[40] S. Wang, Y. Wang, M. Jin, X. D. Gu, and D. Samaras, "Conformal geometry and its applications on 3D shape matching, recognition, and stitching," *IEEE Trans. Pattern Anal. Mach. Intell.*, vol. 29, no. 7, pp. 1209–1220, Jul. 2007.

[41] W. Zeng, Y. Zeng, Y. Wang, X. Yin, X. Gu, and D. Samaras, "3D non-rigid surface matching and registration based on holomorphic differentials," in *Proc. Eur. Conf. Comput. Vis.* Berlin, Germany: Springer, 2008.

[42] L. Ahlfors and L. Bers, "Riemann's mapping theorem for variable metrics," pp. 265–296, 1960.

[43] Y. Zeng, C. Wang, X. Gu, D. Samaras, and N. Paragios, "Higher-order graph principles towards non-rigid surface registration," *IEEE Trans. Pattern Anal. Mach. Intell.*, vol. 38, no. 12, pp. 2416–2429, Dec. 2016.

[44] W. Zeng and X. D. Gu, *Ricci Flow For Shape Analysis and Surface Registration: Theories, Algorithms and Applications*. New York, NY, USA: Springer, 2013.

[45] L. V. Ahlfors, *Complex Analysis*. New York, NY, USA: McGraw-Hill, 1979.

[46] E. Persoon and K.-S. Fu, "Shape discrimination using Fourier descriptors," *IEEE Trans. Syst., Man, Cybern.*, vol. 7, no. 3, pp. 170–179, Mar. 1977.

[47] I. N. Sneddon, *Fourier Transforms*. Chelmsford, MA, USA: Courier Corporation, 1995.

[48] G. D. Smith, *Numerical Solution of Partial Differential Equations: Finite Difference Methods*. Oxford, U.K.: Oxford Univ. Press, 1985.

[49] K. Pearson, "On lines and planes of closest fit to systems of points in space," *Philos. Mag.*, vol. 2, no. 6, pp. 559–572, 1901.

[50] X. Wang and D. Zhang, "A high quality color imaging system for computerized tongue image analysis," *Expert Syst. Appl.*, vol. 40, no. 15, pp. 5854–5866, 2013.

[51] *Numerical Conformal Mapping Software*. Accessed: Jan. 7, 2020. [Online]. Available: https://sites.math.washington.edu/~marshall/zipper.html

[52] *Geometric Processing Package*. Accessed: Jan. 7, 2020. [Online]. Available: https://www.math.cuhk.edu.hk/~lmlui/gpp

[53] P. T. Choi and L. M. Lui, "Fast disk conformal parameterization of simply-connected open surfaces," *J. Sci. Comput.*, vol. 65, no. 3, pp. 1065–1090, 2015.

[54] M. H. Yueh, W. W. Lin, and C. T. Wu, "An efficient energy minimization for conformal parameterizations," *J. Sci. Comput.*, vol. 73, no. 1, pp. 203–227, 2017.

[55] D. I. Barnea and H. F. Silverman, "A class of algorithms for fast digital image registration," *IEEE Trans. Comput.*, vol. C-21, no. 2, pp. 179–186, Feb. 1972.

[56] G. Wolberg and S. Zokai, "Image registration for perspective deformation recovery," *Proc. SPIE*, vol. 4050, pp. 259–270, Aug. 2000.

[57] C. Cortes and V. Vapnik, "Support-vector networks," *Mach. Learn.*, vol. 20, no. 3, pp. 273–297, 1995.

[58] A. W. Whitney, "A direct method of nonparametric measurement selection," *IEEE Trans. Comput.*, vol. C-20, no. 9, pp. 1100–1103, Sep. 1971.
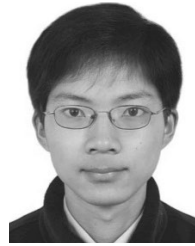
JIAN WU received the B.S. degree in mathematics from Liaoning Normal University, Dalian, China, in 2010, and the M.S. degree in mathematics from Gannan Normal University, Ganzhou, China, in 2014. He is currently pursuing the Ph.D. degree in computer science with the Shenzhen Graduate School, Harbin Institute of Technology at Shenzhen, Shenzhen, China. His research interests focus on medical biometrics, pattern recognition, and image processing.

BOB ZHANG (M'11–SM'19) received the B.A. degree in computer science from York University, Toronto, ON, Canada, in 2006, the M.A.Sc. degree in information systems security from Concordia University, Montreal, QC, Canada, in 2007, and the Ph.D. degree in electrical and computer engineering from the University of Waterloo, Waterloo, ON, Canada, in 2011. He was with the Center for Pattern Recognition and Machine Intelligence and later was a Postdoctoral Researcher with the Department of Electrical and Computer Engineering, Carnegie Mellon University, Pittsburgh, PA, USA. He is currently an Associate Professor with the Department of Computer and Information Science, University of Macau, Macau, China. His research interests focus on biometrics, pattern recognition, and image processing. He is a Technical Committee Member of the IEEE Systems, Man, and Cybernetics Society and an Associate Editor of *IET Computer Vision*.

YONG XU (M'06–SM'15) received the B.S. and M.S. degrees and the Ph.D. degree in pattern recognition and intelligence system from the Nanjing University of Science and Technology, Nanjing, China, in 1994, 1997, and 2005, respectively. He is currently with the Bio-Computing Research Center, Harbin Institute of Technology at Shenzhen, Shenzhen, China. His current research interests include pattern recognition, biometrics, bioinformatics, machine learning, image processing, and video analysis.

DAVID ZHANG (F'08) received the degree in computer science from Peking University, Beijing, China, and the M.Sc. degree in computer science and the Ph.D. degree from the Harbin Institute of Technology (HIT), Harbin, China, in 1982 and 1985, respectively, and the second Ph.D. degree in electrical and computer engineering from the University of Waterloo, Waterloo, ON, Canada, in 1994. From 1986 to 1988, he was a Postdoctoral Fellow with Tsinghua University, Beijing, and then an Associate Professor with Academia Sinica, Beijing. He is currently a Presidential Chair Professor with the School of Science and Engineering, The Chinese University of Hong Kong at Shenzhen, Shenzhen. He also serves as a Visiting Chair Professor with Tsinghua University and also an Adjunct Professor with Peking University, Beijing, Shanghai Jiao Tong University, Shanghai, HIT, and the University of Waterloo. He has authored more than 10 books and 200 journal articles. He is the Founder and the Editor-in-Chief of the *International Journal of Image and Graphics*, a Book Editor of Springer *International Series on Biometrics*, an Organizer of the International Conference on Biometrics Authentication, and an Associate Editor of more than ten international journals, including the IEEE Transactions and *Pattern Recognition*. He is a Croucher Senior Research Fellow, a Distinguished Speaker of the IEEE Computer Society, and a Fellow of IAPR.

● ● ●